CrossMark

JFM PAPERS

Critical selection of shear sheltering in electroconvective flow from chaotic to steady state

Wei Liu[1,2], Yueting Zhou[1,2],† and **Pengpeng Shi[3,4],†**

[1] School of Aerospace Engineering and Applied Mechanics, Tongji University, Shanghai 200092, PR China

[2] Shanghai Key Lab of Vehicle Aerodynamics and Vehicle Thermal Management Systems, Shanghai 201804, PR China

[3] School of Civil Engineering, Xi'an University of Architecture and Technology, Xi'an 710055, Shaanxi, PR China

[4] State Key Laboratory for Strength and Vibration of Mechanical Structures, Shaanxi Engineering Research Centre of NDT and Structural Integrity Evaluation, School of Aerospace, Xi'an Jiaotong University, Xi'an 710049, Shaanxi, PR China

Ion and water are transported by electroconvection near permselective membranes, resulting in complex phenomena associated with the flow–fines interaction. Sheltering the flow chaos by the shear flow is a common strategy in plasma fluids and has recently been successfully applied to control ionic fluids. The paper herein reveals the critical selection of shear velocity regarding the fluid from a chaotic to a steady state through numerical and theoretical analyses. For the shear sheltering, the dimensionless Debye length λ_D with varying channel height is introduced to achieve a comprehensive discussion of the factors and laws affecting the shear vortex state. Based on an analysis of the vortex driving mechanism, the scaling of the slip velocity $u_s \sim (\lambda_D^{-1} \Delta\phi^4)^{1/3}$ is recommended as the critical selection factor for the steady and chaotic state under a fixed shear flow velocity, which involves the dimensionless Debye length λ_D and voltage difference $\Delta\phi$. Furthermore, for ionic fluid control by shear flow, a critical shear velocity U_{HPC} is proposed to distinguish the electroconvective flow from a chaotic state to a steady state. When the shear flow velocity $U_{HP} > U_{HPC}$, the shear flow shelters chaos, and the scaling law is also recommended for the regulation of the critical shear flow velocity U_{HPC} jointly by λ_D and $\Delta\phi$. The analysis is confirmed by direct numerical simulation and existing experimental data (*J. Fluid Mech*, vol. 813, 2017, pp. 799–823). This work provides a more comprehensive physical insight for shear sheltering and affects the design of electromembrane microfluidics.

Key words: electrokinetic flows, microscale transport, instability control

† Email addresses for correspondence: zhouyt@tongji.edu.cn, shipengpeng@xjtu.edu.cn

1. Introduction

Electroconvective flow (ECF) (Rubinstein & Zaltzman 2000) is one of the paradigmatical flows in fluid physics, following the Taylor–Couette flow (Huisman *et al.* 2013), the Rayleigh–Bénard flow (Ahlers, Grossmann & Lohse 2009), the pipe flow (Kühnen *et al.* 2018), etc. To date, there are three possible explanations for the physical mechanism of ECF. One is the non-equilibrium ECF (Zaltzman & Rubinstein 2007) related to the extended space charge (ESC) layer, the other is the equilibrium ECF (Rubinstein & Zaltzman 2015; Aboelkassem 2019; Tripathi, Narla & Aboelkassem 2020; Xu *et al.* 2020) related to the electric double layer and the last is the ECF related to charge injection (Guan, Riley & Novosselov 2020; Luo *et al.* 2020; Su *et al.* 2020). The non-equilibrium ECF associated with the ESC layer, which is typically triggered in electrochemical systems embedded with cation-selective membranes, is considered here, as shown in figure 1. Since the cation-selective membrane is composed of negatively charged nanopore structures, the pore walls attract cations and repel anions, realizing the function of cation-selective permeation. Once the applied voltage reaches a certain threshold, the electrolyte solution forms a steep ion concentration gradient at the interface of the ion-selective membrane, which is the so-called ion concentration polarization (Rubinstein & Zaltzman 2000). Since the first experimental observation in 2008 (Rubinstein *et al.* 2008), the non-equilibrium ECF related to the ESC layer has been studied extensively due to its relevance for desalination (Kim *et al.* 2010; Liu, Zhou & Shi 2020*a*) and preconcentration (Ouyang *et al.* 2018). Non-equilibrium ECFs usually have three typical flow states. When the voltage is low, the flow field in the channel shows typical pressure-flow characteristics. Upon a further increase in voltage, a steady vortex array is formed on the membranes (Liu, Zhou & Shi 2020*b*), which is the so-called overlimiting behaviour. As the voltage increases again, the steady vortex is broken, forming a chaotic ECF (Druzgalski & Mani 2016; Nikonenko *et al.* 2016; Mani & Wang 2020).

For non-shear ECFs, physicists have carried out a series of studies on the statistical characteristics, bifurcation behaviour, spatiotemporal dynamics, buoyancy effects and electrolyte effects. For the statistical characteristics of non-shear ECFs, Druzgalski, Andersen & Mani (2013) and Davidson, Andersen & Mani (2014) found that under high voltage, chaotic vortices appear near the ion selective membranes, which is similar to turbulent transport. Their results show that the chaotic micro-vortex can eject positive and negative free charges into the bulk, forming a completely chaotic multilayer structure with a broadband energy spectrum. When the voltage is cyclically loaded, the ECF presents supercritical bifurcation and subcritical bifurcation. To understand its bifurcation type, Demekhin, Nikitin & Shelistov (2013) and Shelistov, Demekhin & Ganchenko (2014), by linear analysis and direct numerical simulation (DNS), revealed that it is determined by the hydrodynamic coupling coefficient. Subsequently, Pham *et al.* (2012) revealed the physical mechanism of subcritical bifurcation based on DNS and found that the transverse electric field and pressure gradient can maintain the vortex under a voltage lower than the critical value. Yossifon & Chang (2008) studied the intermittent vortex depletion layer on the membrane surface in a slow AC field, showing self-similar diffusion growth. Furthermore, Demekhin, Shelistov & Polyanskikh (2011) found that the chaotic vortex under high voltage prevented the self-similar growth of the diffusion layer and established a wavenumber selection principle. However, these electrochemical systems inherently involve changes in fluid density set by the salt concentration. Once the characteristic length of the system reaches a certain threshold, the concentration-dependent buoyancy effect cannot be ignored. Karatay *et al.* (2016) numerically predicted the coupling effect between the buoyant force and the electrostatic force and found that the flow characteristics
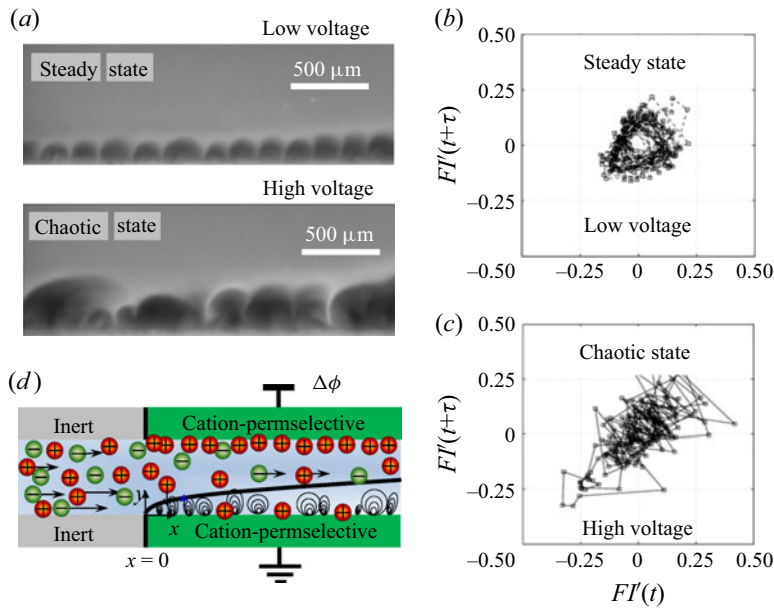
Figure 1. Effect of the voltage difference of the system on the fluid state. (*a*) Flow pattern at different voltages (Kwak *et al.* 2017). Increasing the voltage difference of the system causes the fluid to transition from a steady ECF to a chaotic one. Attractors (Kwak *et al.* 2017) of fluorescence intensity in a time-delay phase space $[FI'(t), FI'(t + \tau)]$ under (*b*) low voltage difference and (*c*) high voltage difference, where τ is the time delay. The visualization of vortices can be achieved by adding small amounts of fluorescent dyes, as the intensity of fluorescent dyes weakens with decreasing local ion concentration. The drop in ion concentration in the ion depletion region is visualized as a dark region, so the state of the vortex can be quantitatively analysed by detecting the intensity change in the dark region of the fluorescent dye. (*d*) Simulation model, which consists of two permselective membranes as well as electrolytes. A vortex depletion zone is formed near the bottom membranes under a vertical electric field.

are similar to the large-scale circulation (Wei & Xia 2013; Wei & Ahlers 2016; Hasan & Gross 2020, 2021) in the Rayleigh–Bénard flow when the buoyant force destabilizes the flow. This coupling effect between the buoyancy and ECF was subsequently confirmed by experiments (de Valenca *et al.* 2017). In many natural scenarios, fluids can also be of the non-Newtonian type, which usually occurs in Li-ion batteries. Li, Archer & Koch (2019) studied the ECF in viscoelastic electrolyte through numerical simulation and found that polymer stretching and shrinking can enhance flow chaos. In addition, these studies found that current oscillations depend on the chaotic fluctuations of vortices (Druzgalski *et al.* 2013; Mani & Wang 2020).

Under the effect of shear flow, the vortex rolls out of the channel with the shear flow, forming a shear ECF. Kwak *et al.* (2013*b*) found that the shear velocity $\tilde{U}_{HP}$ and voltage difference $\Delta\tilde{\phi}$ can jointly regulate the vortex height. Shi & Liu (2018) and Shi (2021) further discussed the length-dependent effect of the vortex height and found that the characteristic length of the channel can achieve a high-precision simulation of vortex height. Kang & Kwak (2020) found that adjusting the voltage and shear flow velocity can realize the switching of polygonal, transverse and longitudinal rolls. However, linear overlimiting behaviour has been observed by experiments (Kwak *et al.* 2013*b*; Kang & Kwak 2020) and simulations (Shi & Liu 2018). Liu *et al.* (2020*b*) subsequently revealed the balance mechanism of convective flux and electrostatic flux and derived the linear law of ion transport efficiency, which can be used to explain the linear overlimiting behaviour.

If the voltage difference of the system is very high, the overlap of vortices can cause the incomplete desalination zone to shrink along the inlet, and the shrinkage law can be described by the scaling $(\Delta\tilde{\phi}^2/\tilde{U}_{HP})^{-1}$ (Liu, Zhou & Shi 2020c). This overlap of vortices apparently determines the upper limit of the overlimiting current, which is consistent with experimental observations (Kwak *et al.* 2013a). Sheltering chaos by shear flow is a common method in plasma fluids and has recently been successfully applied to control the ECF state (Kwak, Pham & Han 2017). Sheared by the horizontal Hagen–Poiseuille flow, the flow chaos of the ECF can be suppressed, which is called shear sheltering. The strength of shear sheltering is dominated by the shear velocity, and the shear sheltering effect strengthens as the shear velocity $\tilde{U}_{HP}$ increases. For the first time, it was found that the flow state can be identified by the critical vortex height, and the scaling of the vortex height satisfies $(\Delta\tilde{\phi}^2/\tilde{U}_{HP})^{1/3}$ in terms of the voltage difference and shear velocity (Kwak *et al.* 2013b). Combining scaling and experiments, the phase diagram of the flow regime regulated by the flow velocity and voltage has also been reported (Kwak *et al.* 2017). For convenience, we extracted the results of previous experiments (Kwak *et al.* 2017). Figure 1(*a*) shows that the voltage difference has a significant enhancement effect on the flow chaos, which is characterized by the attractors in a time-delay phase space. The curves in figures 1(*b*) and 1(*c*) clearly show that increasing the voltage difference can realize the transition from a steady state to a chaotic state.

For the shear sheltering, this paper extends the previous analysis (Kwak *et al.* 2017) and shows that a dimensionless parameter (the dimensionless Debye length λ_D regulated by the channel height) can significantly modulate the shear ECF state, enabling a more comprehensive study on the state selection of shear ECFs. Herein, a new scaling law is found for the critical shear velocity with the dimensionless Debye length and the dimensionless voltage difference. For small λ_D, moderate voltages can cause massively small-scale vortices to be ejected near the permselective membranes, triggering flow chaos. By exploring the parameter space spanned by the dimensional Debye length λ_D, shear velocity U_{HP} and voltage difference $\Delta\phi$, a comprehensive analysis of the factors and laws affecting the fluid state is achieved. Based on theoretical analysis and direct numerical simulations, we find that the steady and chaotic states can be distinguished by the critical slip velocity in a certain shear flow scenario. For ionic fluid control by shear sheltering, the shear flow velocity can achieve the transition of flow from a chaotic to steady state (Kwak *et al.* 2013b, 2017; Liu *et al.* 2020c). By performing balance analysis on the vortex driving mechanism, the scaling law of the critical shear flow velocity U_{HPC} for switching between the chaotic state and the steady state is obtained, which is jointly regulated by the dimensional Debye length λ_D and voltage difference $\Delta\phi$.

2. Theoretical analysis

Non-equilibrium ECF governs the transport of ions, mass, electric potential and momentum on multiple scales. To quantitatively understand the critical selection of shear sheltering in ECF from chaotic to steady state, the following relevant theoretical analysis is performed next in this paper.

2.1. *Problem description and basic equations*

We consider a symmetric binary electrolyte between two cation permselective membranes subject to the applied voltage and the shear flow. Figure 1(*d*) schematically plots the stable vortex at the edge of the ESC layer, where the non-equilibrium ECF governs the transport, voltage and momentum on multiple scales. The shear ECF can be described using the

Poisson–Nernst–Planck (PNP) and incompressible Navier–Stokes (NS) equations. The PNP-NS equations are given in dimensional form:

$$\frac{\tilde{\partial}\tilde{c}_{\pm}}{\tilde{\partial}\tilde{t}} = \tilde{\boldsymbol{\nabla}} \cdot \tilde{\boldsymbol{J}}_{\pm}, \tag{2.1}$$

$$\tilde{\boldsymbol{J}}_{\pm} = \tilde{D}_{\pm}\tilde{\boldsymbol{\nabla}}\tilde{c}_{\pm} \pm \frac{\tilde{D}_{\pm}\tilde{c}_{\pm}\tilde{\boldsymbol{\nabla}}\tilde{\phi}}{\tilde{\phi}_0} - \tilde{U}\tilde{c}_{\pm}, \tag{2.2}$$

$$\tilde{\varepsilon}_0\tilde{\varepsilon}_r\tilde{\nabla}^2\tilde{\phi} = (\tilde{c}_- - \tilde{c}_+)\tilde{F}, \tag{2.3}$$

$$\tilde{\rho}_0\frac{\partial\tilde{U}}{\partial\tilde{t}} + \tilde{\rho}_0\tilde{U}\cdot\tilde{\boldsymbol{\nabla}}\tilde{U} + \check{F}(\tilde{c}_- - \tilde{c}_+)\tilde{\boldsymbol{\nabla}}\tilde{\phi} = -\tilde{\boldsymbol{\nabla}}\tilde{P} + \tilde{\mu}\tilde{\nabla}^2\tilde{U}, \tag{2.4}$$

$$\tilde{\boldsymbol{\nabla}} \cdot \tilde{U} = 0, \tag{2.5}$$

where $\tilde{c}_+$ and $\tilde{c}_-$ denote the concentrations of cations and anions, respectively, and $\tilde{\boldsymbol{J}}_{\pm}$ represent the flux of cations and anions, respectively; $\tilde{t}$ represent the time; $\tilde{D}_+$ and $\tilde{D}_-$ is the diffusion coefficients of cations and anions, respectively; $\tilde{\phi}$ is the electric potential; $\tilde{\phi}_0 = \tilde{k}_B\tilde{T}/\tilde{z}\tilde{e}$ represents the thermal voltage, where $\tilde{T}$ is the temperature, $\tilde{k}_B$ is the Boltzmann's constant, $\tilde{z}$ is the valence and $\tilde{e}$ is the elementary charge; $\tilde{\varepsilon}_0$ is the vacuum permittivity, $\tilde{\varepsilon}_r$ is the relative permittivity constant and $\tilde{F}$ is Faraday's constant. For the NS equations, $\tilde{\rho}_0$ is the density of the fluid, $\tilde{U}$ is the fluid velocity, $\tilde{P}$ is the pressure and $\tilde{\mu}$ is the dynamic viscosity. Note that the non-equilibrium ECF occurs on length scales that are orders of magnitude smaller than macroscopic flows, belonging to the low-Reynolds-number and high-Schmidt-number flows. Therefore, the incompressible Navier–Stokes equation can be further simplified to the Stokes equation. Please refer to Appendix A for details.

To facilitate the solution of the PNP-Stokes equations, this paper adopts the dimensionless form of the governing equations. We scale dimensionless spatial coordinates by the channel height $\tilde{l}_0$, dimensionless time by the diffusion time $\tilde{t}_0 = \tilde{l}_0^2/\tilde{D}_0$, dimensionless concentration by bulk concentration $\tilde{c}_0$, dimensionless pressure by the osmotic pressure $\tilde{P}_0 = \tilde{\mu}\tilde{D}_0/\tilde{l}_0^2$, dimensionless velocity by the diffusion velocity $\tilde{U}_0 = \tilde{D}_0/\tilde{l}_0$ and dimensionless voltage by the thermal voltage $\tilde{\phi}_0$. Here, $\tilde{D}_0$ is the average diffusion coefficient of the ions. The nonlinear coupled equations in dimensionless form read:

$$\frac{\partial c_{\pm}}{\partial t} = \boldsymbol{\nabla} \cdot \boldsymbol{J}_{\pm}, \tag{2.1'}$$

$$\boldsymbol{J}_{\pm} = \boldsymbol{\nabla}c_{\pm} \pm c_{\pm}\boldsymbol{\nabla}\phi - Uc_{\pm}, \tag{2.2'}$$

$$\nabla^2\phi = \frac{c_- - c_+}{\lambda_D^2}, \tag{2.3'}$$

$$\nabla^2 U = -\kappa_0\nabla^2\phi\boldsymbol{\nabla}\phi + \boldsymbol{\nabla}P, \tag{2.4'}$$

$$\boldsymbol{\nabla} \cdot U = 0, \tag{2.5'}$$

in which $c_+, c_-, t, \boldsymbol{J}_{\pm}, \phi, U = (u, v)$ and P are the dimensionless cation concentration, dimensionless anion concentration, dimensionless time, dimensionless fluxes of cations/anions, dimensionless electric potential, dimensionless velocity and dimensionless hydrodynamic pressure, respectively. Here, u and v are the components of dimensionless velocity in the x and y directions, respectively.

In this study, the three significant dimensionless parameters are the dimensionless Debye length, the dimensionless voltage difference and the dimensionless averaged flow velocity

$$\lambda_D = \sqrt{\tilde{\varepsilon}_0 \tilde{\varepsilon}_r \tilde{k}_B \tilde{T} / [(\tilde{z}\tilde{e})^2 \tilde{c}_0]} / \tilde{l}_0, \quad \Delta\phi \quad \text{and} \quad U_{HP}. \quad (2.6a\text{–}c)$$

Here, λ_D denotes the ratio between the dimensional Debye length $\sqrt{\tilde{\varepsilon}_0 \tilde{\varepsilon}_r \tilde{k}_B \tilde{T} / [(\tilde{z}\tilde{e})^2 \tilde{c}_0]}$ and $\tilde{l}_0$, where $\tilde{\varepsilon}_0$ is the vacuum permittivity and $\tilde{\varepsilon}_r$ is the relative permittivity constant. Generally, the pores of an ion-selective membrane are in contact with an aqueous solution, and the interfacial chemistry causes the pore walls to carry a certain number of negative charges. The electrostatic attraction of the pore wall causes the pore wall to attract cations and repel anions and then forms a thin non-zero charge layer on the nanometre scale near the pore surface of the ion-selective membrane, which is called the electric double layer (EDL) (Mani & Wang 2020). The dimensionless Debye length λ_D is mainly regulated by the combined ion concentration $\tilde{c}_0$ and the channel height $\tilde{l}_0$. For the fixed concentration, the characteristic height of the system can be in a wide range, $O(1\,\mu m) \le \tilde{l}_0 \le O(1000\,\mu m)$. Therefore, the dimensionless Debye length can be in the range of $10^{-6} \le \lambda_D \le 10^{-2}$ (Mani & Wang 2020). Here, $\Delta\phi$ describes the voltage difference between the upper and lower ends of the membranes, which is the most essential factor to trigger the ECF; U_{HP} is the average value of the shear flow velocity at the inlet, which describes the strength of shear sheltering. The remaining dimensionless parameter is the hydrodynamic coupling constant $\kappa_0 = \tilde{\phi}_0^2 \tilde{\varepsilon}_0 \tilde{\varepsilon}_r / (\tilde{\eta} \tilde{D}_0)$, which describes the influence of the diffusion coefficient and fluid viscosity in the electrolyte on the ECF. For salt solutions, κ_0 is usually a fixed constant of 0.5, which is widely used in ECF studies (Druzgalski *et al.* 2013; Davidson *et al.* 2014; Druzgalski & Mani 2016; Mani & Wang 2020).

2.2. *Dimensionless boundary conditions*

To obtain solutions for (2.1')–(2.5'), the corresponding boundary conditions are necessary. For the top cation permselective membranes at $y = 1$, we have

$$c_m = c_+ = 2, \quad \boldsymbol{J}_- \cdot \boldsymbol{n} = 0, \quad \phi = \Delta\phi, \quad \boldsymbol{U} = 0. \quad (2.7a\text{–}d)$$

Here, n is the unit normal vector of the boundary. The first term in (2.7a–d), the Dirichlet boundary condition ($c_m = c_+ = 2$), can lead to a solution containing a steep gradient near the cation permselective membranes, forming a depletion layer (Rubinstein & Shtilman 1979). Due to the electrostatic attraction of cations, porous nanostructures within cation-selective membranes result in the membrane surface generally maintaining a fixed cation concentration higher than the bulk concentration value. For simplicity, many physicists have introduced the boundary condition of a fixed dimensionless cation concentration at the membrane surface as $c_m = 2$ (Demekhin *et al.* 2013; Druzgalski *et al.* 2013; Rubinstein *et al.* 2008). We also added the discussion on the different values of fixed cation concentration, and the results show that the effect can be ignored. Please refer to Appendix B. The second term in (2.7a–d) ensures that the anion flux is zero. The third term in (2.7a–d) is the voltage at the top cation membranes, which is to start the ECF. The last item is the well-known no-slip velocity boundary condition.

Similarly, for the bottom cation permselective membrane at $y = 0$, the corresponding boundary conditions are

$$c_m = c_+ = 2, \quad \boldsymbol{J}_- \cdot \boldsymbol{n} = 0, \quad \phi = 0, \quad U = 0. \tag{2.8a–d}$$

For the inlet boundary at $x = 0$, we use the following boundary conditions of fixed ion concentration and pressure flow

$$c_\pm = 1, \quad u = 6U_{HP}y(1 - y). \tag{2.9a,b}$$

For the outlet boundary at $x = 3$, we adopt the outflow boundary condition since both ion and fluid flow out of the channel,

$$\nabla c_\pm \cdot \boldsymbol{n} = 0, \quad \nabla U \cdot \boldsymbol{n} = 0. \tag{2.10a,b}$$

2.3. *Critical selection of shear sheltering*

It is well known that the vortex roll is triggered by the electroosmotic slip velocity u_s at the edge of the ESC layer. Therefore, analysis of the slip velocity is expected to yield a quantitative understanding of fluid state selection. A previous study (Druzgalski *et al.* 2013) has implied that the increase in slip velocity can promote the overall growth of the vortex, forming a steady vortex. If the slip velocity further increases and reaches a threshold, the fluid transitions from a steady state to a chaotic state. Subsequently, the critical slip velocity can be used to distinguish the flow states, which is confirmed by DNS. Therefore, the critical slip velocity is recommended as the direct cause of the fluid state. The Stokes equation in the non-equilibrium double layer can be simplified to the following form (Rubinstein & Zaltzman 2001)

$$\frac{\partial^2 u}{\partial y^2} \sim \frac{1}{2}\frac{\partial}{\partial x}\left(\frac{\partial \phi}{\partial y}\right)^2 - \left(\frac{\partial}{\partial y}\frac{\partial \phi}{\partial y}\right)\frac{\partial \phi}{\partial x} \quad \text{for } 0 \leq y \leq y_{ESC}. \tag{2.11}$$

The non-equilibrium double layer carries a high non-zero space charge density distribution within it, which is also called the ESC layer (Rubinstein & Zaltzman 2001; Mani & Wang 2020). Here, u denotes the velocity distribution inside the ESC layer ($0 \leq y \leq y_{ESC}$) and y_{ESC} is the length of the ESC layer; see figure 2(*a*). In (2.11), the first term on the right-hand side, $\frac{1}{2}(\partial/\partial x)(\partial \phi/\partial y)^2$, describes the contribution of the pressure driving force to the slip velocity, while the second term, $-((\partial/\partial y)(\partial \phi/\partial y))(\partial \phi/\partial x)$, describes the contribution of the electrostatic driving force within the ESC layer to the slip velocity. However, the effect of κ_0 on the slip velocity can be neglected because κ_0 of the salt solution is a fixed constant of 0.5 (Druzgalski *et al.* 2013; Davidson *et al.* 2014; Druzgalski & Mani 2016; Mani & Wang 2020).

To obtain the expression of the velocity by integrating (2.11) twice, the solution of ϕ must be analysed first. With the one-dimensional (1-D) quiescent steady-state solutions for the electric field, the PNP equation can be transformed into a nonlinear ordinary differential equation (Rubinstein & Zaltzman 2001; Zaltzman & Rubinstein 2007),

$$\lambda_D^2 \frac{d^2 E}{dy^2} = \frac{1}{2}E^3 + j(y - y_{ESC})E + \lambda_D j, \tag{2.12}$$

where the normalized electric field E denotes $-\lambda_D(d\phi/dy)$, and the current j is defined as $dc_+/dy + c_+(d\phi/dy)$. The physical parameters satisfy $E = O(1/\lambda_D)$ and $d/dy = O(1)$
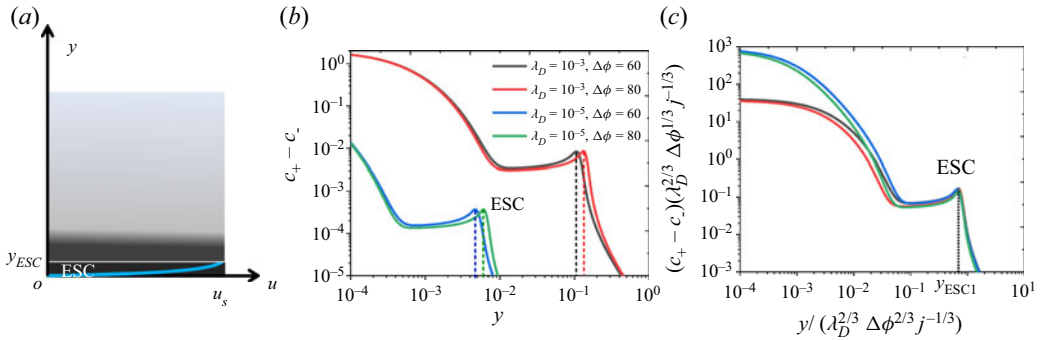
Figure 2. ESC structure and velocity distribution. (*a*) Schematic diagram of the model for the ESC layer, where the slip velocity is defined as the velocity at the edge of the ESC layer, as shown by the blue line. (*b*) ESC layer structure at different voltages and dimensionless Debye layer lengths. The vicinity of the membrane–solution interface is in a 1-D quasi-steady state and is occupied by the ESC layer. This thickness exceeds its dimensionless Debye layer length by 2–3 orders of magnitude. (*c*) Scaling behaviour of the 'convex peak' in the ESC layer. Using scaling laws $y_{ESC} \sim \lambda_D^{2/3} \Delta\phi^{2/3} j^{-1/3}$ and $c_+ - c_- \sim \lambda_D^{2/3} \Delta\phi^{1/3} j^{-1/3}$, the scattered 'convex peaks' in the ESC layer fold at one point.

with reference to the dimensionless Debye layer length λ_D. Then, (2.12) turns into the cubic algebraic equation (Demekhin *et al.* 2015)

$$0 \sim \tfrac{1}{2}E^3 + j(y - y_{ESC})E = E[\tfrac{1}{2}E^2 + j(y - y_{ESC})] \quad \text{for } 0 \leq y \leq y_{ESC}. \tag{2.13}$$

The ESC layer carries a non-negative high electric field. Then, the solution of (2.13) is $\tfrac{1}{2}E^2 + j(y - y_{ESC}) \sim 0$, yielding $E^2 \sim 2j(y_{ESC} - y)$. Using $E = -\lambda_D(\mathrm{d}\phi/\mathrm{d}y)$, the leading solution of E in the ESC layer is

$$\lambda_D^2 \left(\frac{\mathrm{d}\phi}{\mathrm{d}y}\right)^2 \sim 2j(y_{ESC} - y) \quad \text{for } 0 \leq y \leq y_{ESC}. \tag{2.14}$$

Equation (2.14) can also be obtained from (2.12) by the asymptotic expansion of

$$E = -\lambda_D \frac{\mathrm{d}\phi}{\mathrm{d}y} = -\sqrt{2j(y_{ESC} - y)} - \frac{\lambda_D}{2(y_{ESC} - y)} + \cdots \tag{2.15}$$

(Rubinstein & Zaltzman 2001). In the ESC layer, the leading solution of E is $\lambda_D(\mathrm{d}\phi/\mathrm{d}y) \sim \sqrt{2j(y_{ESC} - y)}$, which is consistent with the dimensional analysis. Equation (2.14) can effectively analyse the electric field distribution within the ESC layer, which is widely adopted by many studies (Rubinstein & Zaltzman 2001; Zaltzman & Rubinstein 2007; Demekhin *et al.* 2015). Integrating (2.14), one can obtain the leading solution of the voltage distribution inside the ESC layer,

$$\phi \sim \frac{2\sqrt{2}}{3} \lambda_D^{-1} j^{1/2} [y_{ESC}^{3/2} - (y_{ESC} - y)^{3/2}] \quad \text{for } 0 \leq y \leq y_{ESC}. \tag{2.16}$$

To obtain the expression of the velocity, bringing (2.16) into (2.11) yields

$$\frac{\partial^2 u}{\partial y} \sim \lambda_D^{-2}(y_{ESC} - y)\frac{\partial j}{\partial x} + \lambda_D^{-2} j \frac{\partial y_{ESC}}{\partial x} - \frac{1}{3}\lambda_D^{-2}(y_{ESC} - y)\frac{\partial j}{\partial x} - \lambda_D^{-2} j \frac{\partial y_{ESC}}{\partial x}$$

$$+ \frac{1}{3}\frac{1}{\sqrt{y_{ESC} - y}}\lambda_D^{-2} y_{ESC}^{\frac{3}{2}}\frac{\partial j}{\partial x} + \lambda_D^{-2} j \frac{y_{ESC}^{\frac{1}{2}}}{\sqrt{y_{ESC} - y}}\frac{\partial y_{ESC}}{\partial x} \quad \text{for } 0 \leq y \leq y_{ESC}. \tag{2.17}$$

In (2.17), $\lambda_D^{-2}(y_{ESC} - y)(\partial j/\partial x) + \lambda_D^{-2}j(\partial y_{ESC}/\partial x)$ is derived from the pressure driving force $\frac{1}{2}(\partial/\partial x)(\partial\phi/\partial y)^2$, while the last four terms at the right end of (2.17) are derived from the electrostatic driving force $-((\partial/\partial y)(\partial\phi/\partial y))(\partial\phi/\partial x)$. Simplifying (2.17), we have

$$\frac{\partial^2 u}{\partial y^2} \sim \frac{2}{3}\lambda_D^{-2}(y_{ESC} - y)\frac{\partial j}{\partial x} + \frac{1}{3}\frac{1}{\sqrt{y_{ESC} - y}}\lambda_D^{-2}y_{ESC}^{3/2}\frac{\partial j}{\partial x}$$
$$+\lambda_D^{-2}j\frac{y_{ESC}^{1/2}}{\sqrt{y_{ESC} - y}}\frac{\partial y_{ESC}}{\partial x} \quad \text{for } 0 \le y \le y_{ESC}. \tag{2.18}$$

In (2.18), the contribution of the pressure driving force to the slip velocity is offset by the contribution of part of the volume force, resulting in the pressure driving force dominant term $\frac{2}{3}\lambda_D^{-2}(y_{ESC} - y)(\partial j/\partial x)$. Similarly, the contribution of the electrostatic driving force to the slip velocity is offset by part of the pressure driving force, resulting in the electrostatic driving force dominant term

$$\frac{1}{3}\frac{1}{\sqrt{y_{ESC} - y}}\lambda_D^{-2}y_{ESC}^{3/2}\frac{\partial j}{\partial x} + \lambda_D^{-2}j\frac{y_{ESC}^{1/2}}{\sqrt{y_{ESC} - y}}\frac{\partial y_{ESC}}{\partial x}. \tag{2.19}$$

By integrating (2.18) twice and applying the boundary conditions $\partial u/\partial y = 0$ for $y = y_{ESC}$ and $u = 0$ for $y = 0$, we have

$$u_s = u(y = y_{ESC}) \sim -\frac{1}{9}\lambda_D^{-2}y_{ESC}^3\frac{\partial j}{\partial x} - \frac{4}{9}\lambda_D^{-2}y_{ESC}^3\frac{\partial j}{\partial x} - \frac{4}{3}\lambda_D^{-2}jy_{ESC}^2\frac{\partial y_{ESC}}{\partial x}. \tag{2.20}$$

Here, the slip velocity at the edge of the ESC layer is denoted by u_s.

Further analysis is needed to obtain a concise form of the scaling law of u_s. Assuming that the voltage at the ESC layer is ϕ_{ESC}, and using $\phi(y = y_{ESC}) - \phi(y = 0) = \phi_{ESC}$, the leading solution can be obtained for the length of the ESC layer,

$$y_{ESC} \sim \frac{\sqrt[3]{9}}{2}\lambda_D^{2/3}\phi_{ESC}^{2/3}j^{-1/3} \sim \lambda_D^{2/3}\Delta\phi^{2/3}j^{-1/3}. \tag{2.21}$$

To confirm the validity of the above analysis of the length of the ESC layer, we assume that the voltage ϕ_{ESC} at the edge of the ESC layer is approximately equal to the anode voltage $\Delta\phi$. Therefore, the scaling of the length of the ESC layer can be expressed as $y_{ESC} \sim \lambda_D^{2/3}\Delta\phi^{2/3}j^{-1/3}$, where j can be calculated from the current density. In figure 2(*b*), by identifying the location of the 'convex peak', the length of the ESC layer can be obtained. The charge density of the 'convex peak' is also analysed. In the electrically neutral region, the ion concentration decreases linearly, and we can obtain $c_+ \sim j(y - y_{ESC})$. For the ESC layer, the anion concentration is almost 0, yielding $c_+ - c_- \sim \lambda_D^2(d^2\phi/dy^2) \sim \lambda_D^2\Delta\phi/(y - y_{ESC})^2$. Considering $c_+ - c_- \sim c_+$ in the ESC layer, one has $c_+ - c_- \sim c_+ \sim \lambda_D^2\Delta\phi/(c_+/j)^2$. One can obtain the scaling of the charge density, $c_+ - c_- \sim \lambda_D^{2/3}\Delta\phi^{1/3}j^{-1/3}$. Using scalings $c_+ - c_- \sim \lambda_D^{2/3}\Delta\phi^{1/3}j^{-1/3}$ and $y_{ESC} \sim \lambda_D^{2/3}\Delta\phi^{2/3}j^{-1/3}$, the scattered 'convex peaks' collapse at one point, as shown in figure 2(*c*). The above analysis confirms the validity of the low-order approximation, which allows the analysis of the velocity at the edge of the ESC layer.

Using $y_{ESC} \sim (\sqrt[3]{9}/2)\lambda_D^{2/3}\phi_{ESC}^{2/3}j^{-1/3}$ yields

$$u_s \sim -\frac{1}{8}\phi_{ESC}^2 j^{-1}\frac{\partial j}{\partial x} - \phi_{ESC}\frac{\partial\phi_{ESC}}{\partial x}. \tag{2.22}$$

The above analysis allows one to more clearly understand the physical meaning of the slip velocity u_s. The first term $-\frac{1}{8}\phi_{ESC}^2 j^{-1}(\partial j/\partial x)$ of (2.22) is contributed mainly by the

pressure driving force ∇P, whereas the second term $-\phi_{ESC}(\partial\phi_{ESC}/\partial x)$ is contributed mainly by the electrostatic driving force $\nabla^2\phi\nabla\phi$. Therefore, the slip velocity u_s depends on the joint contribution of the pressure driving force ∇P and the electrostatic driving force $\nabla^2\phi\nabla\phi$ within the ESC layer.

To obtain the scaling form of (2.22), the following three assumptions are adopted (Kwak *et al.* 2017): (i) the slip velocity of the ESC edge is equal to the outermost vortex velocity of the ECF; (ii) the vortex is a hemisphere, that is, the vortex width is substantially equal to the vortex height and (iii) the voltage ϕ_{ESC} at the ESC edge is $\Delta\phi$. A previous study showed that the ion flux satisfies the relation $j \approx \partial c_+/\partial y$ (Rubinstein & Zaltzman 2000), so $j^{-1}(\partial j/\partial x)$ can be further simplified as $j^{-1}(\partial j/\partial x) \approx (\partial^2 c_+/\partial x\partial y)/(\partial c_+/\partial y)$. Using a first-order approximation $1/\partial x \sim 1/\partial y \sim 1/\delta_0$, $(\partial^2 c_+/\partial x\partial y)/(\partial c_+/\partial y)$ can be further simplified as$\sim 1/\delta_0$, where the depletion layer thickness δ_0 can be identified by a given vortex height d_{EC}. Furthermore, the slip velocity can be estimated by $u_s \sim \Delta\phi^2(1/\delta_0)$ (Kwak *et al.* 2017), which is proven to be valid for analysing the slip velocity of non-shear flows (Liu *et al.* 2020*b*). However, for the shear shielding case, the slip velocity is dominated by the shear flow velocity. Considering that the vortex height and shear velocity satisfy the scaling, the vortex height satisfies $\delta \sim \delta_0 U_{HP}^{-1/3}$ (Kwak *et al.* 2017; Nakayama *et al.* 2017), and a modified first-order approximation $(1/\partial x \sim 1/\partial y \sim 1/\delta/U_{HP}^{-1/3})$ with the shear flow is used. Referring to the existing scaling $\tilde{d}_{EC}/\tilde{l}_0 = \tilde{C} \cdot \Delta\tilde{\phi}^{2/3}\tilde{U}_{HP}^{-1/3}$ (Kwak *et al.* 2013*b*), a more reasonable scaling $\tilde{d}_{EC}/\tilde{l}_0 = \tilde{C}_1 \cdot \Delta\tilde{E}^{2/3}\tilde{U}_{HP}^{-1/3}$ is recommended for the length-dependent effect (Shi & Liu 2018), where both $\tilde{C}$ and $\tilde{C}_1$ are the dimensional fitting coefficients, and $\Delta\tilde{E} = \Delta\tilde{\phi}/\tilde{l}_0$ is the average external electric field. Based on the dimensionless references, one can obtain that $\tilde{d}_{EC}/\tilde{l}_0 = \tilde{C}_1\tilde{\phi}_0^{2/3}\tilde{D}_0^{-1/3}\tilde{l}_0^{-1/3}(\Delta\tilde{\phi}/\tilde{\phi}_0)^{2/3}(\tilde{U}_{HP}/\tilde{D}_0/\tilde{l}_0)^{-1/3}$. For the case of the constant dimensional Debye length and given permselective membranes, the length-dependent effect is essentially determined by the dimensionless Debye length effect (Mani & Wang 2020). Further, one can get $d_{EC} \sim \lambda_D^{1/3}\Delta\phi^{2/3}U_{HP}^{-1/3}$ to consider the length-dependent λ_D effect, where the dimensionless fitting coefficient is $C_1 = \tilde{C}_1(\tilde{\phi}_0/\tilde{\lambda}_D)^{2/3}(\tilde{D}_0/\tilde{\lambda}_D)^{-1/3}$. Then, (2.22) can be converted into a universal scaling,

$$u_s \sim U_{HP}^{-1/3}(-\tfrac{1}{8}\Delta\phi^2 d_{EC}^{-1} - \Delta\phi^2 d_{EC}^{-1}) \sim (\lambda_D^{-1}\Delta\phi^4)^{1/3}. \tag{2.23}$$

Scaling (2.23) implies that the slip velocity is mainly contributed by $\phi_{ESC}(\partial\phi_{ESC}/\partial x) \sim \Delta\phi^2 d_{EC}^{-1}$, which may be important for the flow analysis. More importantly, one can understand the dimensionless Debye length λ_D mismatch leading to the slope mismatch problem of vortex growth in simulation and experiment; please refer to figure 2 in Kwak *et al.* (2013*b*) or figure 3 in Shi & Liu (2018). Scaling (2.23) demonstrates that the driving force for slip velocity originates from the electrostatic force at the edge of the ESC layer, which is discussed in detail in Appendix C.

Scaling (2.23) indicates that the slip velocity is not only regulated by the well-known voltage difference $\Delta\phi$ but also affected by the dimensionless Debye length λ_D. Combined with figure 2, the dimensionless Debye layer length λ_D describes the effect of the ESC layer thickness (adjusted by λ_D) on the slip velocity, and $\Delta\phi$ describes the effect of the external voltage. Our analysis also implies that the flow state is controlled jointly by the dimensionless voltage difference $\Delta\phi$ and the dimensionless Debye length λ_D. In the discussion section, we will confirm that reducing the dimensionless Debye length λ_D can enhance flow chaos.

For fluid controlled by shear flow, increasing the shear flow velocity U_{HP} can lead to a transition from a chaotic to a steady-state fluid, which is called shear sheltering (Kwak

et al. 2017). To quantitatively understand how shear sheltering regulates chaotic and steady states, the criterion of the strong-shear limit ($\epsilon_s = u_s/\delta y u_y$) is adopted (Terry 2000; Kwak *et al.* 2017). The equivalent scaling form of the strong-shear limit is $u_s = \epsilon_s \delta y u_y \sim \delta y u_y$. Here, u_s is the electro-osmotic slip velocity of the vortex; δy is the region away from the flow shear, which is scaled by the critical vortex boundary layer thickness δ_c and u_y is the mean flow shear, which is scaled by $U_{HP}/(1 - \delta_c)$. Consequently, the critical selection between chaotic and steady states can be described as

$$u_y \sim u_s/\delta_c. \tag{2.24}$$

Scaling (2.24) establishes a balance relation between the average intensity of shear flow velocity u_y and the average intensity of slip velocity u_s/δ_c at critical vortex height δ_c. A previous study (Kwak *et al.* 2017) suggested that the critical selection of the flow state is determined by the critical vortex height δ_c. Therefore, the scaling of the critical shear velocity U_{HPC} between the chaotic state and the steady state can be expressed as

$$U_{HPC} \sim \frac{1 - \delta_c}{\delta_c} u_s \sim (\lambda_D^{-1} \Delta \phi^4)^{1/3}. \tag{2.25}$$

Scaling (2.25) is the core result for the critical selection of shear sheltering, revealing the joint regulation of the dimensionless Debye length λ_D and the dimensionless voltage difference $\Delta \phi$ to the critical shear velocity U_{HPC}. When the shear flow velocity U_{HP} reaches above a critical shear flow velocity U_{HPC}, the flow chaos is suppressed. However, when the shear flow velocity is below a critical shear flow velocity U_{HPC}, the flow is chaotic. Then, the fluid state in parameter space (λ_D, $\Delta \phi$, and U_{HP}) is explored by DNS to achieve a comprehensive analysis of the flow state.

3. Discussion

For simplicity, a non-equilibrium ECF with symmetric and binary ($z_\pm = \pm 1$) electrolytes of equal diffusivities ($D_\pm = 1$) is studied here. The key dimensionless parameters selected are $10^{-6} \leq \lambda_D \leq 10^{-2}$, $240 \leq U_{HP} \leq 1000$ and $0 \leq \Delta \phi \leq 120$. We consider the case of the given bulk concentration where the value of λ_D can span several orders of magnitude, which is caused by the channel height $O(10)[\mu m] \leq \tilde{l}_0 \leq O(1000)[\mu m]$ (Shi & Liu 2018; Mani & Wang 2020).

To confirm the above theoretical analysis, we numerically explored the parameter space spanned by the dimensional Debye length λ_D, voltage difference $\Delta \phi$ and shear velocity U_{HP} to determine the accuracy of our scaling. Equations (2.1')–(2.5') and the corresponding boundary conditions (2.7)–(2.10) are solved based on the finite element method in the two-dimensional (2-D) rectangular domain. To accurately capture the fine changes in various physical quantities in the vortex near the cation permselective membrane, a large number of quadrilateral grids are arranged in the EDL $O(\lambda_D)$ and ESC layers $O(\lambda_D^{2/3})$. The simulation time is $O(0.1)$, at which time the non-equilibrium ECF has fully developed. In our simulation, the time step is selected as $O(10^{-7})$ to ensure convergence in the transient calculation. For more finite element details, please refer to our previous work (Shi & Liu 2018; Liu *et al.* 2020c; Xu *et al.* 2020).

3.1. *Debye layer effect for the shear vortex state*

In figure 3, we plot the effect of different dimensionless Debye lengths λ_D on the flow state under a fixed voltage difference $\Delta \phi = 40$. Upon decreasing the dimensionless
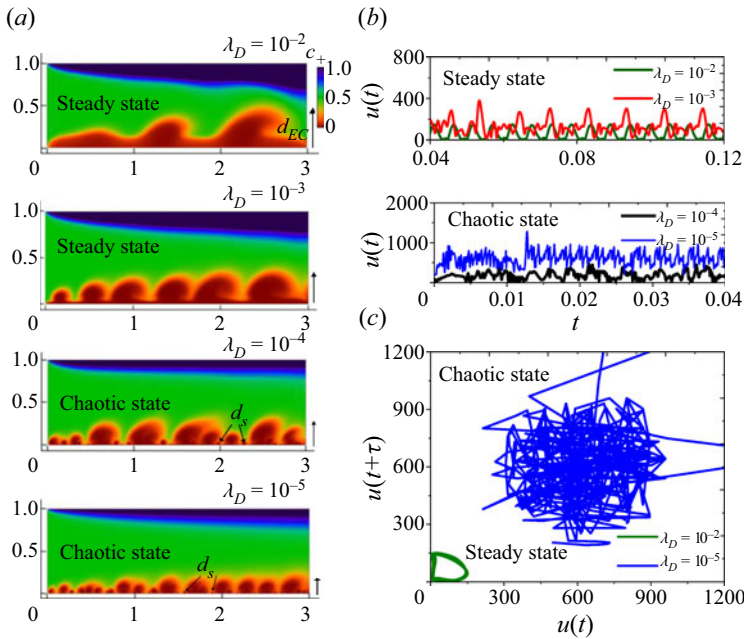
Figure 3. Effect of the dimensionless parameter λ_D on the fluid state. (*a*) Surface instantaneous snapshots show the fully developed salt concentration for various λ_D. The blue colours show the ion enrichment regime emerging from the top cation permselective membranes, while the red colours show the depletion vortices formations near the bottom cation permselective membranes. (*b*) Instantaneous velocity profiles at the monitoring points $(x, y) = (2.5, \ y_{ESC})$ for various λ_D. (*c*) Slip velocity attractors in a time-delay phase space. As the dimensionless Debye length λ_D decreases, the velocity fluctuation of the ESC layer becomes more chaotic, indicating that λ_D can significantly regulate the flow state. The local small-scale vortices d_s need to be magnified several times for viewing. Here, $\Delta\phi = 40$ and $U_{HP} = 240$.

Debye length λ_D, massive small-scale vortices are ejected near the cation permselective membrane, forming an irregular concentration boundary layer structure. These figures imply that the flow chaos is not only affected by the well-known voltage difference $\Delta\phi$ but is also significantly modulated by the dimensionless factor λ_D. The periodic-to-chaotic transition is determined from the delay-time phase diagram, which has been successfully used to identify the flow states (Kwak *et al.* 2017). To quantitatively describe fluid chaos, velocity attractors are adopted in a time-delay phase space. The velocity spatiotemporal fluctuation curves at a point $(x, y) = (2.5, \ y_{ESC})$ at the edge of the ESC layer and the slip velocity attractors $[u(t + \tau), u(\tau)]$ in a time-delay phase space are presented in figures 2(*b*) and 2(*c*), respectively. Here, τ is the time delay. These attractors clearly reveal that reducing λ_D can cause the flow to move from a steady state to a chaotic state.

At the small dimensionless Debye length λ_D scenario, we identify a distinct transitional pathway to the chaotic state that does not feature the conventional chaos bursts (Kwak *et al.* 2017) and instead proceeds via the characteristics of the ESC layer. Physically, decreasing the dimensionless Debye length can weaken the ESC layer thickness $(\lambda_D^{2/3})$ and enhance the electrostatic driving force $(\nabla^2\phi\nabla\phi \sim \phi^2/d_{EC}^3)$, resulting in small-scale vortices erupting. These small-scale vortices interact in a complicated manner through the shear flow, which eventually leads to fluid chaos. As a result, the slip velocity increases with decreasing dimensionless Debye length λ_D. Consequently, a transition to flow chaos can occur via two distinctly different pathways, namely, (i) through increasing the voltage

difference $\Delta\phi$ (Kwak *et al.* 2013*a,b*, 2017) and (ii) through decreasing the dimensionless Debye length λ_D (see figure 3). This implies that the fluid state is regulated by the combination of voltage difference $\Delta\phi$ and dimensionless Debye length λ_D at a fixed shear flow velocity. Even though the pathways to the chaotic state can be different, there may be a universal criterion, the critical slip velocity of the vortex. Next, for a fixed shear flow velocity scenario, based on the DNS and scaling, we explore how the dimensionless Debye length λ_D and voltage difference $\Delta\phi$ jointly regulate the flow state and slip velocity.

3.2. *Slip velocity for the shear vortex*

For a microfluidic system with permselective membranes, the critical factor of the flow state is recommended at a fixed shear flow velocity scenario. Our analysis has shown that increasing the voltage difference $\Delta\phi$ or decreasing the dimensionless Debye length λ_D can enhance the chaos and slip velocity. It is well known that the slip velocity u_s at the edge of the ESC layer is the most basic driving factor that drives the vortex to roll. Consequently, the slip velocity u_s is expected to yield a quantitative understanding of the selection of the flow state. Using the scaling $(\lambda_D^{-1}\Delta\phi^4)^{1/3}$, we found that the scattered data in figure 4(*b*) all collapse on a straight line,

$$u_s = \alpha \cdot (\lambda_D^{-1}\Delta\phi^4)^{1/3}. \tag{3.1}$$

Here, the theoretical analysis is performed for the configuration with a fixed shear flow velocity $U_{HP} = 240$. In this scenario, the fitting coefficient α is 0.12. Figure 4(*a*) supports the reliability of our scaling analysis. Further analysis of the slip velocity shows that the selection of the flow state can be distinguished by the critical value of slip velocity u_{cri}, and its value is approximately 210. The increase in the slip velocity can promote the overall growth of the vortex, forming a steady vortex structure with a regular charge layer, as shown in figure 4(*b*). With this fixed shear flow velocity, however, the slip velocity further reached a critical value ($\sim$210), the vortex became overwhelmed, and an irregular charge layer structure was formed. From this perspective, the critical slip velocity u_{cri} is recommended as the critical selection factor for the steady and chaotic states. Based on the scaling $u_s \sim (\lambda_D^{-1}\Delta\phi^4)^{1/3}$, a lower voltage difference $\Delta\phi$ is required in the smaller λ_D scenario for the chaotic state.

Based on the above numerical analysis, the slip velocity is recommended as a key factor for the critical selection of the flow state. Using the critical value of slip velocity u_{cri}, the instability phase diagram related to λ_D and $\Delta\phi$ is obtained (see figure 5*a*). In the scenario of a fixed shear flow, once the input parameters (λ_D and $\Delta\phi$) of the system are above the critical line, the flow is chaotic. Our DNS data support this analysis (see figure 5*b*). Consequently, for a larger λ_D, a higher voltage difference is required for the flow to maintain the chaotic state since the driving force $-\nabla^2\phi\nabla\phi + \nabla P$ of the ESC layer is smaller. From the perspective of the slip velocity, a larger slip velocity can lead to the onset of the chaotic state.

For real electrochemical systems, scaling (3.1) can be rewritten as an alternative form, $\tilde{u}_s \sim \tilde{l}_0^{1/3}\Delta\tilde{\phi}^{4/3}$, which is jointly regulated by the key physical parameters of the system input. Increasing the channel height $\tilde{l}_0$ and voltage difference $\Delta\tilde{\phi}$ can enhance the instability. In fact, the channel height $\tilde{l}_0$ and the voltage difference $\Delta\tilde{\phi}$ can span several orders of magnitude, such as $O(10)[\mu m] < \tilde{l}_0 < O(10^3)[\mu m]$ and $O(10)[mV] < \Delta\tilde{\phi} < O(10^3)[mV]$. More generally, voltage difference regulation is the most common strategy for enhancing flow chaos, appearing in many ECF studies (Demekhin *et al.* 2013; Kwak
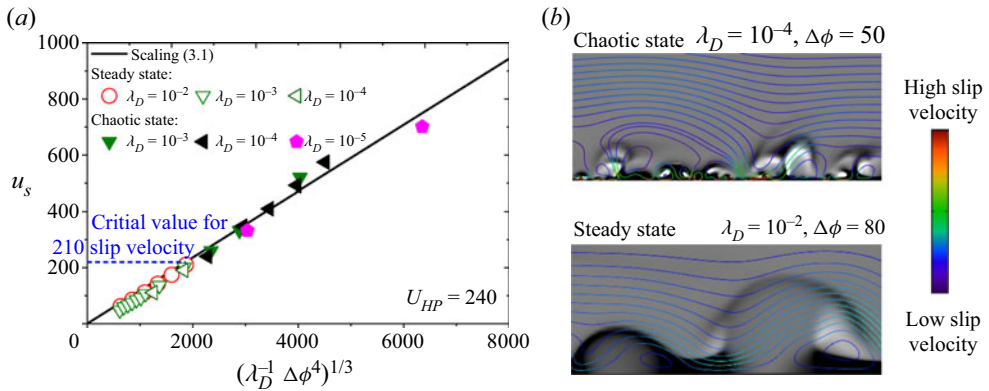
Figure 4. Slip velocity scaling. (*a*) Slip velocity of the vortex plotted against the scaling factor $(\lambda_D^{-1}\Delta\phi^4)^{1/3}$. The data points are all extracted from figure 5(*b*). Here, the slip velocity u_s is defined as the time average $u_s = (1/(t_1 - t_0)) \int_{t_0}^{t_1} \sqrt{u^2 + v^2}\, dt$ of the velocity at the edge of the ESC layer, where t_0 is the initial time and t_1 is the cut-off time after the EC flow is fully developed. (*b*) Snapshot plots show the ESC layer superimposed with streamlines. In the scenario of high slip velocity, the area corresponding to the red streamline at the edge of ESC layer (need to be enlarged to view), the membrane surface ejects the chaotic multilayer charge boundary layer structure. However, the slip velocity is below the critical slip velocity, forming a steady flow, which corresponds to the streamlined blue area in the bottom picture of figure 4(*b*). Here, $U_{HP} = 240$.
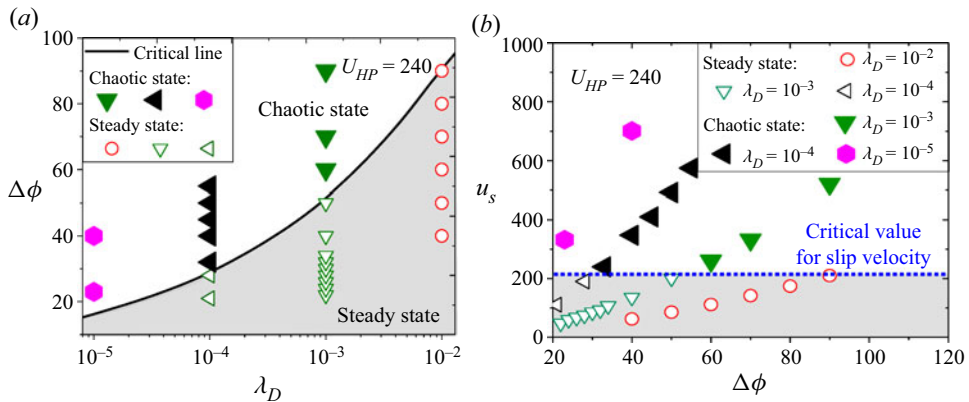
Figure 5. Joint regulation of the flow state and slip velocity by λ_D and $\Delta\phi$. (*a*) Critical selection of ECF from steady to chaotic state for phase diagram replotted in dimensionless numbers: $\Delta\phi$ versus λ_D. The black curve is expressed as the critical line, $\Delta\phi = (u_{cri}/\alpha)^{3/4}\lambda_D^{1/4}$, which is calculated by scaling (3.1). For a larger λ_D, a larger voltage difference $\nabla\phi$ can reach the chaotic state. (*b*) Effect of $\Delta\phi$ and λ_D on the slip velocity. The blue dashed line marks the slip velocity threshold, above which the flow is chaotic. Here, $U_{HP} = 240$.

et al. 2013*b*, 2017; Shelistov *et al.* 2014). Controlling the flow state is conducive to guiding the design of desalination systems and electrodeposition.

3.3. *Critical shear velocity for the shear sheltering*

For fluid control, applying external shear flow is a common method to suppress flow chaos and has recently been successfully used to control the ECF state (Kwak *et al.* 2017). In this section, the results of § 3.2 are further extended to describe the critical parameter values of the flow state under various shear flow velocities. In figure 6(*a*), we plot the flow
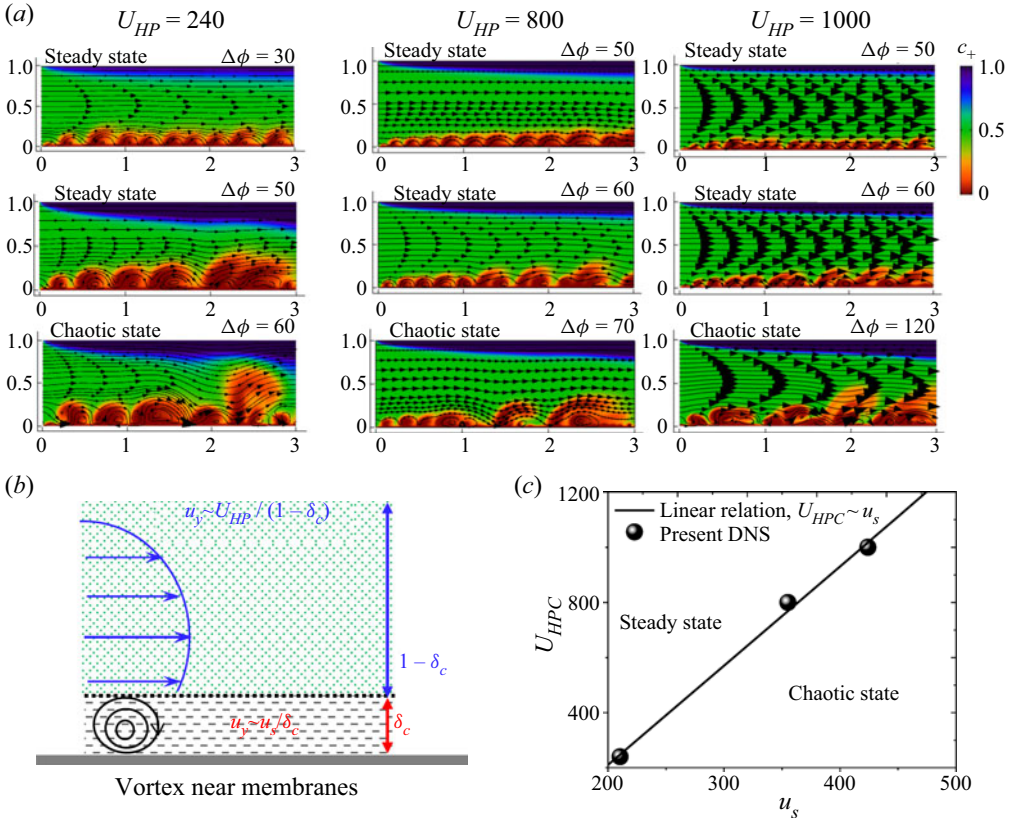
Figure 6. Shear sheltering. Surface instantaneous snapshots show the cation concentration field and flow field structure for different shear flow velocities. Increasing the shear flow velocity can shelter chaos, whereas increasing the voltage difference can enhance chaos. Flow states are identified by slip velocity attractors; see Appendix D. (*b*) Balance mechanism of velocity average intensity. (*c*) Linear relation between the shear flow velocity and the slip velocity. Here, $\lambda_D = 10^{-3}$.

patterns at different shear flow velocities. Increasing the shear velocity U_{HP}, the chaotic vortex is suppressed by the shear flow, forming a regular oblique structure. For larger shear flow velocities, a large voltage difference is required to trigger flow chaos, as shown in figure 6(*a*).

Based on the shear limit criterion (Terry 2000; Kwak *et al.* 2017), the critical balance relation $U_{HPC}/(1 - \delta_c) \sim u_s/\delta_c$ between the average intensity of the shear flow velocity and the average intensity of the vortex slip velocity is obtained (see figure 6*b*). Consequently, the critical shear velocity and slip velocity satisfy an approximately linear relation $U_{HPC} \sim ((1 - \delta_c)/\delta_c)u_s$ but are disturbed by the prefactor coefficient $(1 - \delta_c)/\delta_c$. However, previous studies suggested that the steady state and chaotic state can be distinguished by the critical thickness δ_c of the vortex boundary layer, and its value is 0.309 (Kwak *et al.* 2017). This indicates that δ_c is basically fixed for shear sheltering. Ignoring the disturbance prefactor coefficient $(1 - \delta_c)/\delta_c$, a simple linear scaling ($U_{HPC} \sim u_s$) is obtained (see figure 6*c*). This approximately linear scaling is confirmed by DNS. Consequently, the chaotic state is characterized by high slip velocity, which indicates that a larger shear velocity is required to shelter chaos. By exploring the shear velocity and slip velocity under the parameter space (λ_D, $\Delta\phi$ and U_{HP}), one can further understand the
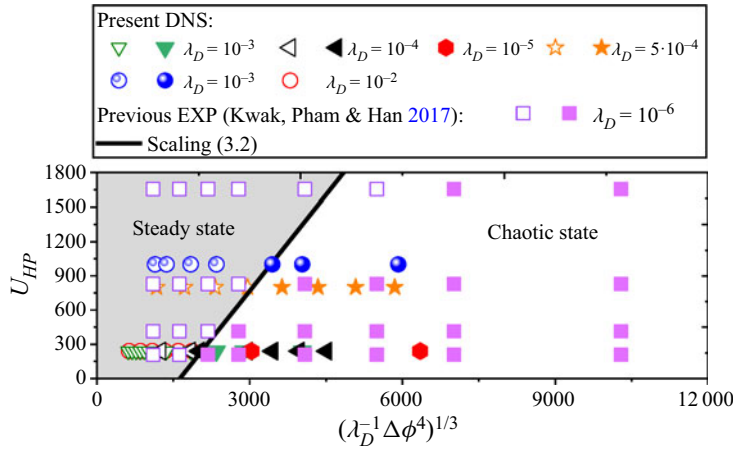
946 A3-15

Figure 7. Critical shear velocity for shear sheltering. Critical selection of ECF from steady to chaotic state for phase diagram replotted in dimensionless numbers: $(\lambda_D^{-1}\Delta\phi^4)^{1/3}$ versus U_{HP}. The dimensionless Debye layer length λ_D describes the effect of the ESC length (regulated by the dimensionless Debye layer length) on the flow state, $\Delta\phi$ depicts the effect of the voltage difference and the shear velocity U_{HP} characterizes the shear shielding. For convenience, two regional colours are used to distinguish the flow state. The chaotic state is maintained by the large slip velocity, and a larger shear flow velocity is required to suppress the chaos. Here, we extracted all experimental data (Kwak *et al.* 2017) under the dimensionless Debye length $\lambda_D = 10^{-6}$ with various shear flow velocities [$U_{HP} = 207(2.5 \ \mu\text{l/min})$, $U_{HP} = 414(5 \ \mu\text{l/min})$, $U_{HP} = 828(10 \ \mu\text{l/min})$ and $U_{HP} = 1656(20 \ \mu\text{l/min})$].

critical shear velocity required for chaos suppression. Please refer to Appendix C for more details.

Based on the above theory and numerical analysis, the fluid state is adjusted by the dimensional Debye length λ_D, shear velocity U_{HP} and voltage difference $\Delta\phi$. As the scaling factor $(\lambda_D^{-1}\Delta\phi^4)^{1/3}$ increases, the fluid state is dominated by electrostatic force, and fluid chaos is enhanced. However, increasing the shear velocity, the flow is dominated by the pressure flow, and the flow chaos is suppressed. Using the scaling relation $U_{HPC} \sim u_s$, a universal phase diagram for shear sheltering can be obtained. Hence, one can obtain the scaling of the critical shear velocity,

$$U_{HPC} = c \cdot (\lambda_D^{-1}\Delta\phi^4)^{1/3} + \xi. \tag{3.2}$$

For a given dimensional Debye length, the present parameter space ($10^{-6} \leq \lambda_D \leq 10^{-2}$, $240 \leq U_{HP} \leq 1000$ and $0 \leq \Delta\phi \leq 120$), the fitting coefficients are $c = 0.56$ and $\xi = 912.87$. Finally, the data in figures 4–6 and experimental data (Kwak *et al.* 2017) are replotted in the phase diagram composed of $(\lambda_D^{-1}\Delta\phi^4)^{1/3}$ and U_{HP}. In figure 7, the two states of the flow are successfully distinguished by a theoretical straight line. This analysis is supported by DNS data and experimental data (Kwak *et al.* 2017). In addition, note that an effective voltage difference $\Delta\phi = \gamma\varphi$ was introduced in multilayer electrodialysis, where $\Delta\phi$ is the voltage difference between the membrane, φ is the total voltage in multilayer electrodialysis and γ describes the resistance effect in multilayer electrodialysis. Therefore, the coefficient γ is assumed to be 0.042 to consider the effective voltage difference caused by the resistance effect of multilayer electrodialysis. Once the shear flow velocity $U_{HP} > U_{HPC}$, the shear flow shelters the chaos. However, when $U_{HP} < U_{HPC}$, the electrostatic force destabilizes the steady flow.

946 A3-16

4. Conclusion

In summary, for a given dimensional Debye length scenario, this work investigates the critical selection between the steady state and chaotic state in an overlimiting electrodialysis channel embedded with two permselective membranes. The main conclusions are as follows.

(i) The theoretical analysis shows that the flow state is adjusted by a new dimensionless factor, the channel height-dependent λ_D. In the overlimiting state, shear ECF usually has two states, including a stable state and a chaotic state. Decreasing λ_D can enhance the electrostatic driving force, and many small-scale vortices are ejected near the membrane, resulting in a chaotic state.

(ii) In the scenario of fixed shear flow velocity, the scaling analysis and DNS find that the slip velocity is the direct cause of the switching between the stable and chaotic states. Based on the scaling law of critical slip velocity, the distinction between steady and chaotic states can be achieved.

(iii) For ionic fluid control by shear sheltering, the critical shear velocity relation $U_{HPC} = c(\lambda_D^{-1} \Delta\phi^4)^{1/3} + \xi$ is obtained. When the shear flow velocity is above the critical shear velocity U_{HPC}, the shear flow shelters the chaotic fluctuations, resulting in the transition of the flow from the chaotic state to the steady state. Existing experimental data (Kwak *et al.* 2017) and our DNS results support the analysis.

These results allow one to quantitatively understand the fluid state and velocity statistics in the ECF and provide optimization guidance for the performance design of electromembrane microfluidic systems, such as desalination (Chuang *et al.* 2020), mixing (Guan, Yang & Wu 2021), preconcentration (Qiu *et al.* 2019), charge injection (Guan & Novosselov 2019) and electrodeposition (Chen *et al.* 2016; Zheng *et al.* 2020). In addition, our scaling analysis is performed on the case with the fixed dimensional Debye length, which is a limitation of the hypothetical scenario. Just for the non-shear electroosmotic flow, the effects of bulk concentration on the mixing efficiency (Peng & Li 2015), flow pattern (Aboelkassem 2019; Tripathi *et al.* 2020) and enrichment efficiency (Ouyang *et al.* 2018) are investigated. Similarly, the concentration effect of the shear electroconvective flow may be interesting, and the experimental and theoretical studies on it deserve to be conducted in the future.

Author ORCIDs.

ⓘ Wei Liu https://orcid.org/0000-0003-0844-0804;

ⓘ Yueting Zhou https://orcid.org/0000-0003-1783-3669;

ⓘ Pengpeng Shi https://orcid.org/0000-0001-8329-809X.

Appendix A. Stokes flow for electrokinetic microfluidics

ECF belongs to the low-*Re*-number flow, and the analysis of fluids based on the Stokes equation is a widely used simplified scheme (Davidson *et al.* 2014; Druzgalski & Mani 2016; Liu *et al.* 2020c; Mani & Wang 2020). The Stokes equation is adopted for the

flow analysis in this paper. The corresponding simplification process is as follows. The dimensional form of the momentum equation is

$$\tilde{\rho}_0 \frac{\partial \tilde{U}}{\partial \tilde{t}} + \rho_0 \tilde{U} \cdot \tilde{\nabla} \tilde{U} = -\tilde{\nabla} \tilde{P} + \tilde{\mu} \tilde{\nabla}^2 \tilde{U} + \tilde{F}(\tilde{c}_- - \tilde{c}_+)\tilde{\nabla}\tilde{\phi}. \quad (A1)$$

To numerically solve these equations, the governing equations should be converted to the dimensionless form. Based on the dimensionless references in the main text, one can obtain the following dimensionless form of the Navier–Stokes equation,

$$\frac{1}{Sc} \frac{\partial U}{\partial t} + Re U \cdot \nabla U = -\nabla^2 U + \nabla P - \kappa_0 \nabla^2 \phi \nabla \phi. \quad (A2)$$

Here, $Sc = \tilde{\mu}/\tilde{\rho}_0 \tilde{D}$ is the Schmidt number and $Re = \tilde{U}_0 \tilde{l}_0 \tilde{\rho}_0/\tilde{\mu}$ is the Reynolds number. The definitions of the remaining parameters and symbols are listed in the main text.

Here, a simplified NS equation is used in the simulation. By ignoring the first two terms $((1/Sc)(\partial U/\partial t) + Re U \cdot \nabla U)$ in (A2), it can be simplified to the Stokes equation,

$$\nabla^2 U = -\kappa_0 \nabla^2 \phi \nabla \phi + \nabla P. \quad (A3)$$

The non-equilibrium ECF belongs to low-Reynolds-number and high-Schmidt-number flows. Therefore, the first two items $((1/Sc)(\partial U/\partial t) + Re U \cdot \nabla U)$ in (A3) can be ignored in this study. By referring to the magnitude of the experimental parameters of the electrodynamic microfluidic device (Kwak *et al.* 2017), the magnitude of the *Re* number and the Schmidt number of the ECF can be calculated as follows.

$$\left. \begin{array}{l} Re = \tilde{U}_0 \dfrac{\tilde{l}_0 \tilde{\rho}_0}{\tilde{\mu}} = \dfrac{10^{-9} \left[\dfrac{\text{m}^2}{\text{s}}\right]}{500\,[\text{mm}]} \cdot 500\,[\text{mm}] \cdot \dfrac{10^3 \left[\dfrac{\text{kg}}{\text{m}^3}\right]}{10^{-3}\,[\text{Pa}\cdot\text{s}]} = 0.001 \\[20pt] Sc = \dfrac{\tilde{\mu}}{\tilde{\rho}_0 \tilde{D}_0} = \dfrac{10^{-3}\,[\text{Pa}\cdot\text{s}]}{10^3 \left[\dfrac{\text{kg}}{\text{m}^3}\right] \cdot 10^{-9} \left[\dfrac{\text{m}^2}{\text{s}}\right]} = 1000 \end{array} \right\}. \quad (A4)$$

To further confirm that this simplified theory is reasonable, the comparison of the numerical simulation results of the flow field structure is given based on the Navier–Stokes equation (A2) and the simplified Stokes equation (A3), as shown in figure 8. From the streamline (black line) and ion concentration distribution in figure 8, the Stokes equation (A3) can well capture the flow behaviour.

Appendix B. Effect of membrane concentration on the slip velocity

For simplicity, many physicists have introduced the boundary condition of a fixed dimensionless cation concentration at the membrane surface as $c_m = 2$ (Rubinstein *et al.* 2008; Demekhin *et al.* 2013; Druzgalski *et al.* 2013). The boundary condition of different given values of the membrane concentration is also considered in ECF (Green 2020). Here, the effect of different values of membrane concentration c_m on the ECF is discussed. Through DNS, the effect of membrane concentration on flow is analysed, including the flow pattern, slip velocity and extended space charge layer. In figure 9, although the spatiotemporal evolution of the flow pattern is modulated by the membrane concentration, the spatiotemporal average of the vortex slip velocity has not yet been affected. In figure 9, although the spatiotemporal evolution of the flow pattern is modulated by the membrane
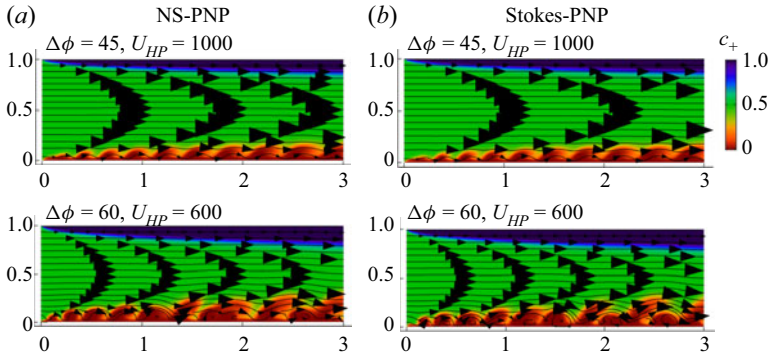
Figure 8. Snapshots of the dimensionless salt concentration with flow streamlines superposed for $\lambda = 5 \times 10^{-4}$. (*a*) DNS results based on the NS-PNP model; (*b*) DNS based on the Stokes-PNP model.
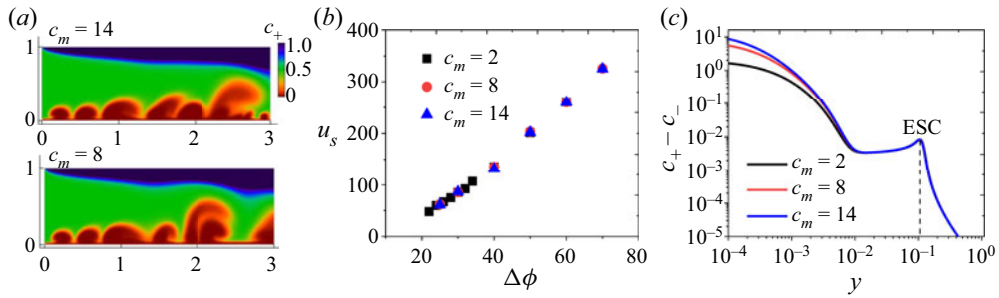

Figure 9. Effect of membrane concentration on flow. (*a*) Effect of membrane concentration on the flow pattern at $\Delta\phi = 60$. (*b*) Average slip velocity at different membrane concentrations and voltage differences. (*c*) ESC layer distribution at different membrane concentrations. Here, $\lambda_D = 10^{-3}$ and $U_{HP} = 240$.

concentration c_m, the average of the vortex slip velocity has not yet been affected. Since the slip velocity of the vortex originates from the electrostatic force at the edge of the ESC layer, it does not depend on the external shear flow. Therefore, the slip velocity of the vortex is closely related to the thickness of the ESC layer. In figure 9(*c*), the distribution of the ECS layer at different membrane concentrations is analysed. It is shown that the thickness of the ESC layer is independent of the membrane concentration c_m, which implies that the slip velocity is independent of the membrane concentration under the situation of statistical stationarity (see figure 9*b*). However, the membrane concentration only modulates the value of the charge density in the EDL, which leads to some differences in the spatiotemporal evolution of the vortex pattern. Our scaling shows that the ESC layer thickness satisfies the scaling relation, $\lambda_D^{2/3} \phi_{ESC}^{2/3} j^{-1/3}$. This indicates that the membrane concentration is independent of the ESC thickness, and therefore, the time average of the slip velocity is independent of the membrane concentration, as shown in figure 9(*b*).

Appendix C. Analysis of the shear velocity and slip velocity

Figure 10(*a*) presents the flow patterns under two sets of shear velocities, the spatiotemporal fluctuations of the slip velocity and the slip velocity attractors. It is shown that the time averaging of slip velocity is almost independent of shear flow but that vortex height and velocity fluctuations can be adjusted. Therefore, an increase in shear flow velocity can suppress the flow disturbance but hardly affect the spatiotemporal average of
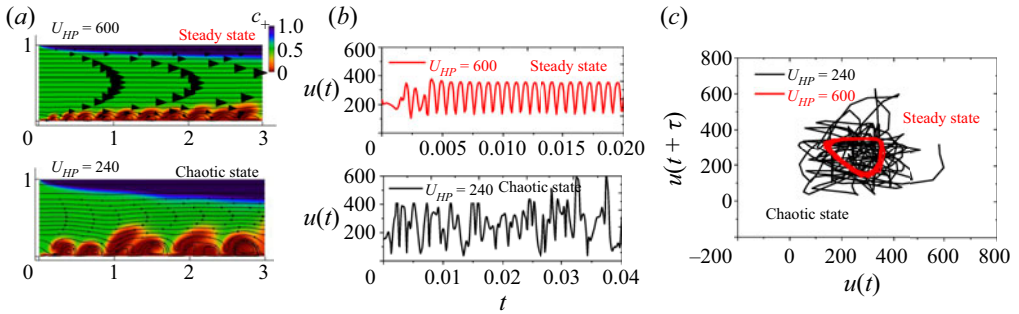
Figure 10. Effect of shear velocity on flow. Shear flow velocity modulates (*a*) flow pattern, (*b*) spatiotemporal fluctuations and (*c*) velocity attractors. Here, $\lambda_D = 10^{-3}$ and $\Delta\phi = 60$.
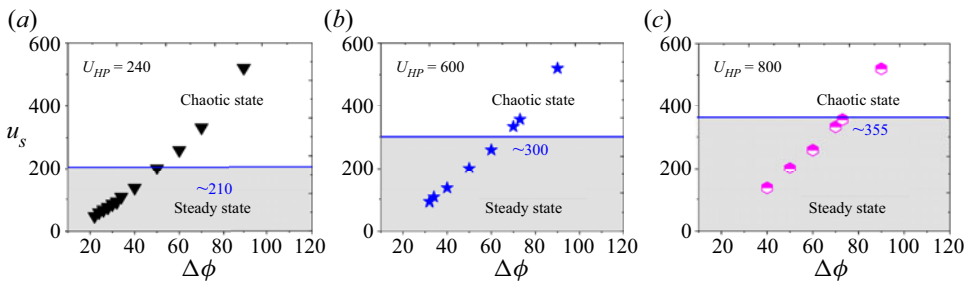

Figure 11. Slip velocity for (*a*) $U_{HP} = 240$, (*b*) $U_{HP} = 600$ and (*c*) $U_{HP} = 800$. An increase in shear flow velocity results in a higher onset voltage of flow chaos. Here, $\lambda_D = 10^{-3}$.

the slip velocity, since the slip velocity originates from the electrostatic force at the edge of the expanding space charge layer, rather than the external shear flow. In figure 10(*b*), the time-averaged speeds are 260 and 265, and this slight change can be ignored.

We also count the slip velocities at various shear flow velocities, as shown in figure 11. As the shear flow velocity increases, the critical voltage for triggering the chaotic state is higher. For a fixed shear flow velocity, the critical slip velocity required for the chaotic state is universal. When the shear flow velocity is set to 240, a critical slip velocity ($\sim$210) is required to trigger flow chaos; see figure 11(*a*). As discussed in the main text, the slip velocity is also affected by the dimensionless Debye layer length. Although reducing the dimensionless Debye layer length can enhance the slip velocity and flow chaos, the slip velocity required for the flow to enter the chaotic state is universal, at approximately 210; see figures 3 and 4. In figure 11, the shear flow velocity increases further, and the onset voltage of the flow chaos increases. Once the shear ECF is dominated by electrostatic forces, the electrostatic force destabilizes the steady flow.

The scaling (3.1) suggests that the slip velocity is regulated by the dimensionless Debye layer length λ_D. The scaling coefficient $\alpha = 0.12$ is confirmed to be independent of the shear flow velocity. In figure 13(*a*), we analyse the effect of shear flow velocity on slip velocity for the dimensionless Debye layer length ($\lambda_D = 5 \times 10^{-4}$) scenario. For the larger shear flow velocity scenario $U_{HP} = 1000$, there is a slight change in the slip velocity. Using the scaling $0.12(\lambda_D^{-1}\Delta\phi^4)^{1/3}$, it is found that the scattered data in figures 11 and 12(*a*) all collapse on a straight line, as shown in figure 12(*b*). These analyses show that in the present parameter space, $0.12(\lambda_D^{-1}\Delta\phi^4)^{1/3}$ can basically reveal the evolution law of slip velocity. That is, the fitting coefficient $\alpha = 0.12$ is independent of the shear velocity.
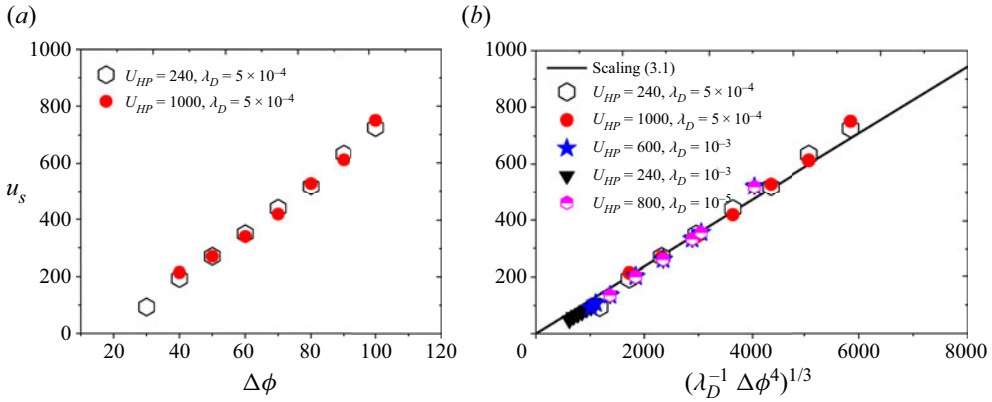
946 A3-20

Figure 12. Slip velocity. (*a*) Effect of $\Delta\phi$ and λ_D on the slip velocity. (*b*) Scaling behaviour of the slip velocity. The slip velocity of the vortex is plotted against the scaling $0.12(\lambda_D^{-1}\Delta\phi^4)^{1/3}$, which shows that the coefficient $\alpha = 0.12$ is independent of the shear flow velocity U_{HP} in the present parameter space.
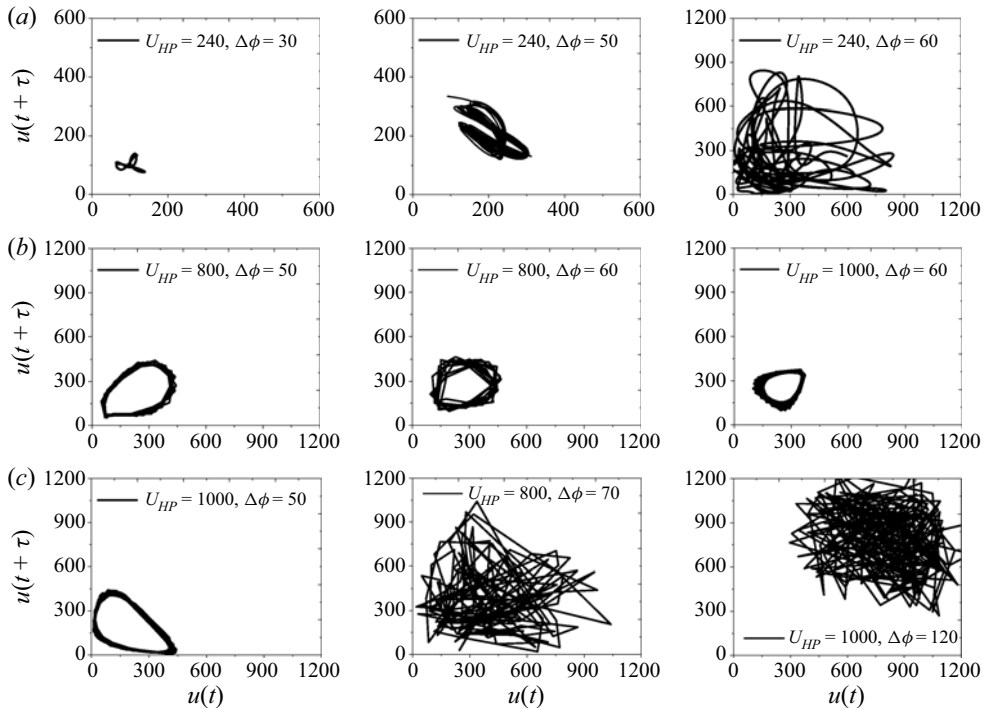

Figure 13. Slip velocity attractors in a time-delay phase space for (*a*) $U_{HP} = 240$, (*b*) $U_{HP} = 800$ and (*c*) $U_{HP} = 1000$. Based on these delay time phase diagrams, the flow state of figure 6(*a*) in the main text is determined. Here, $\lambda_D = 10^{-3}$.

Appendix D. The attractors in a time-delay phase space

To identify the flow states in figure 13(*a*), the attractors in a time-delay phase space (Kwak *et al.* 2017) are used. By analysing the attractor of slip velocity to identify the transition from chaotic to stable flow, one can quantitatively describe how the transition from chaotic sequence to periodic sequence of slip velocity is caused by shear flow. The time series of

slip velocities are recorded to fix a point at the edge of the ESC layer, and delay time phase diagrams of these time series are plotted to determine the flow state of figure 6(*a*), as shown in figure 13.

REFERENCES

ABOELKASSEM, Y. 2019 Pumping flow model in a microchannel with propagative rhythmic membrane contraction. *Phys. Fluids* **31** (5), 51902.

AHLERS, G., GROSSMANN, S. & LOHSE, A.D. 2009 Heat transfer and large scale dynamics in turbulent Rayleigh-Bénard convection. *Rev. Mod. Phys.* **81** (2), 503.

CHEN, Q., ZHU, H., YAN, Z., JU, J.W., JIANG, Z. & WANG, Y. 2016 A multiphase micromechanical model for hybrid fiber reinforced concrete considering the aggregate and ITZ effects. *Const. Build. Mater.* **114**, 839–850.

CHUANG, J.N., DIAO, P.Y., HUANG, W.S., HUANG, L.F., SENAPATI, S., CHANG, H.C. & SUN, Y.M. 2020 Novel homogeneous anion exchange membranes for reproducible and sensitive nucleic acid detection via current–voltage characteristic measurement. *ACS Appl. Mater. Interfaces* **12** (49), 54459–54472.

DAVIDSON, S.M., ANDERSEN, M.B. & MANI, A. 2014 Chaotic induced-charge electro-osmosis. *Phys. Rev. Lett.* **112** (12), 128302.

DE VALENCA, J.C., KURNIAWAN, A., WAGTERVELD, M.R., WOOD, J.A. & LAMMERTINK, R.G.H. 2017 Influence of Rayleigh-Bénard convection on electrokinetic instability in overlimiting current conditions. *Phys. Rev. Fluids* **2** (3), 033701.

DEMEKHIN, E.A., AMIROUDINE, S.G., GANCHENKO, S. & KHASMATULINA, N.Y. 2015 Thermoelectro-convection near charge-selective surfaces. *Phys. Rev.* E **91** (6), 063006.

DEMEKHIN, E.A., NIKITIN, N.V. & SHELISTOV, V.S. 2013 Direct numerical simulation of electrokinetic instability and transition to chaotic motion. *Phys. Fluids* **25** (12), 122001.

DEMEKHIN, E.A., SHELISTOV, V.S. & POLYANSKIKH, S.V. 2011 Linear and nonlinear evolution and diffusion layer selection in electrokinetic instability. *Phys. Rev.* E **84** (3), 036318.

DRUZGALSKI, C.L., ANDERSEN, M.B. & MANI, A. 2013 Direct numerical simulation of electroconvective instability and hydrodynamic chaos near an ion-selective surface. *Phys. Fluids* **25** (11), 110804.

DRUZGALSKI, C.L. & MANI, A. 2016 Statistical analysis of electroconvection near an ion-selective membrane in the highly chaotic regime. *Phys. Rev. Fluids* **1** (7), 073601.

GREEN, Y. 2020 Approximate time-dependent current-voltage relations for currents exceeding the diffusion limit. *Phys. Rev.* E **101** (4), 043113.

GUAN, Y. & NOVOSSELOV, I. 2019 Two relaxation time lattice Boltzmann method coupled to fast Fourier transform Poisson solver: application to electroconvective flow. *J. Comput. Phys.* **397**, 108830.

GUAN, Y.F., RILEY, J. & NOVOSSELOV, I. 2020 Three-dimensional electroconvective vortices in cross flow. *Phys. Rev.* E **101** (03), 033103.

GUAN, Y., YANG, T. & WU, J. 2021 Mixing and transport enhancement in microchannels by electrokinetic flows with charged surface heterogeneity. *Phys. Fluids* **33** (4), 042006.

HASAN, M.K. & GROSS, A. 2020 Temporal secondary stability simulation of Rayleigh–Benard–Poiseuille flow. *Intl J. Heat Mass Transfer* **159**, 120098.

HASAN, M.K. & GROSS, A. 2021 Numerical instability investigation of inward radial Rayleigh–Benard–Poiseuille flow. *Phys. Fluids* **33** (3), 034120.

HUISMAN, S.G., SCHARNOWSKI, S., CIERPKA, C., KAHLER, C.J., LOHSE, A.D. & SUN, C. 2013 Logarithmic boundary layers in strong Taylor-Couette turbulence. *Phys. Rev. Lett.* **110** (26), 264501.

KANG, S. & KWAK, R. 2020 Pattern formation of three-dimensional electroconvection on a charge selective surface. *Phys. Rev. Lett.* **124** (15), 154502.

KARATAY, E., ANDERSEN, M.B., WESSLING, M. & MANI, A. 2016 Coupling between buoyancy forces and electroconvective instability near ion-selective surfaces. *Phys. Rev. Lett.* **116** (19), 194501.

KIM, S.J., KO, S.H., KANG, K.H. & HAN, J. 2010 Direct seawater desalination by ion concentration polarization. *Nat. Nanotechnol.* **5** (4), 297–301.

KÜHNEN, J., SONG, B., SCARSELLI, D., BUDANUR, N.B., RIEDL, M., WILLIS, A.P., AVILA, M. & HOF, B. 2018 Destabilizing turbulence in pipe flow. *Nat. Phys.* **14** (14), 386–390.

KWAK, R., GUAN, G., PENG, W.K. & HAN, J. 2013*a* Microscale electrodialysis: concentration profiling and vortex visualization. *Desalination* **308**, 138–146.

KWAK, R., PHAM, V.S. & HAN, J. 2017 Sheltering the perturbed vortical layer of electroconvection under shear flow. *J. Fluid Mech.* **813**, 799–823.

KWAK, R., PHAM, V.S., LIM, K.M. & HAN, J. 2013*b* Shear flow of an electrically charged fluid by ion concentration polarization: scaling laws for electroconvective vortices. *Phys. Rev. Lett.* **110** (11), 114501.

Li, G., Archer, L.A. & Koch, D.L. 2019 Electroconvection in a viscoelastic electrolyte. *Phys. Rev. Lett.* **122** (12), 12450.

Liu, W., Zhou, Y. & Shi, P. 2020*a* Electrokinetic ion transport at micro–nanochannel interfaces: applications for desalination and micromixing. *Appl. Nanosci.* **10** (3), 751–776.

Liu, W., Zhou, Y. & Shi, P. 2020*b* Scaling laws of electroconvective flow with finite vortex height near permselective membranes. *Phys. Rev.* E **102** (3), 033102.

Liu, W., Zhou, Y. & Shi, P. 2020*c* shear electroconvective instability in electrodialysis channel under extreme depletion and its scaling laws. *Phys. Rev.* E **101** (4), 043105.

Luo, K., Wu, J., Yi, H.L. & Tan, H.P. 2020 Numerical analysis of two-phase electrohydrodynamic flows in the presence of surface charge convection. *Phys. Fluids* **32** (12), 123606.

Mani, A. & Wang, K.M. 2020 Electroconvection near electrochemical interfaces: experiments, modeling, and computation. *Annu. Rev. Fluid Mech.* **52**, 509–529.

Nakayama, A., Sano, Y., Bai, X. & Tado, K. 2017 A boundary layer analysis for determination of the limiting current density in an electrodialysis desalination. *Desalination* **404**, 41–49.

Nikonenko, V.V., Vasil'eva, V.I., Akberova, E.M., Uzdenova, A.M., Urtenovb, M.K., Kovalenko, A.V., Pismenskaya, N.P., Mareev, S.A. & Pourcelly, G. 2016 Competition between diffusion and electroconvection at an ion-selective surface in intensive current regimes. *Adv. Colloid Interface Sci.* **235**, 233–246.

Ouyang, W., Ye, X.H., Li, Z.R. & Han, J. 2018 Deciphering ion concentration polarization-based electrokinetic molecular concentration at the micro-nanofluidic interface: theoretical limits and scaling laws. *Nanoscale* **10** (32), 15187–15194.

Peng, R. & Li, D. 2015 Effects of ionic concentration gradient on electroosmotic flow mixing in a microchannel. *J. Colloid Interface Sci.* **440**, 126–132.

Pham, V.S., Li, Z.R., Lim, K.M., White, J.K. & Han, J. 2012 Direct numerical simulation of electroconvective instability and hysteretic current-voltage response of a permselective membrane. *Phys. Rev.* E **86** (4), 046310.

Qiu, B.L., Gong, L.Y., Li, Z.R. & Han, J. 2019 Electrokinetic flow in the U-shaped micro-nanochannels. *Theor. Appl. Mech. Lett.* **9** (1), 36–42.

Rubinstein, S.M., Manukyan, G., Staicu, A., Rubinstein, I., Zaltzman, B., Lammertink, R.G.H., Mugele, F. & Wessling, M. 2008 Direct observation of a nonequilibrium electro-osmotic instability. *Phys. Rev. Lett.* **101**, 236101.

Rubinstein, I. & Shtilman, L. 1979 Voltage against current curves of cation exchange membranes. *J. Chem. Soc. Faraday Trans.* **75**, 231–246.

Rubinstein, I. & Zaltzman, B. 2000 Electro-osmotically induced convection at a permselective membrane. *Phys. Rev.* E **62**, 2238–2251.

Rubinstein, I. & Zaltzman, B. 2001 Electro-osmotic slip of the second kind and instability in concentration polarization at electrodialysis membranes. *Math. Models Meth. Appl. Sci.* **11** (2), 263–300.

Rubinstein, I. & Zaltzman, B. 2015 Equilibrium electroconvective instability. *Phys. Rev. Lett.* **114**, 114502.

Shelistov, V.S., Demekhin, E.A. & Ganchenko, G.S. 2014 Electrokinetic instability near charge-selective hydrophobic surfaces. *Phys. Rev.* E **90** (1), 013001.

Shi, P. 2021 Direct numerical simulation of electroconvection with thin Debye layer matching canonical experiments. *Phys. Fluids* **33** (3), 032015.

Shi, P. & Liu, W. 2018 Length-dependent instability of shear electroconvective flow: from electroconvective instability to Rayleigh-Bénard instability. *J. Appl. Phys.* **124** (20), 204304.

Su, Z.G., Zhang, Y.M., Luo, K. & Yi, H.L. 2020 Instability of electroconvection in viscoelastic fluids subjected to unipolar injection. *Phys. Fluids* **32** (10), 104102.

Terry, P.W. 2000 Suppression of turbulence and transport by sheared flow. *Rev. Mod. Phys.* **72**, 109–165.

Tripathi, D., Narla, V.K. & Aboelkassem, Y. 2020 Electrokinetic membrane pumping flow model in a microchannel. *Phys. Fluids* **32** (8), 082004.

Wei, P. & Ahlers, G. 2016 On the nature of fluctuations in turbulent Rayleigh-Benard convection at large Prandtl numbers. *J. Fluid Mech.* **802**, 203–244.

Wei, P. & Xia, K.Q. 2013 Viscous boundary layer properties in turbulent thermal convection in a cylindrical cell: the effect of cell tilting. *J. Fluid Mech.* **720**, 140–168.

Xu, B., Gu, Z., Liu, W., Huo, P., Zhou, Y., Rubinstein, S.M., Bazant, M.Z., Zaltzman, B., Rubinstein, I. & Deng, D. 2020 Electro-osmotic instability of concentration enrichment in curved geometries for an aqueous electrolyte. *Phys. Rev. Fluids* **5** (9), 091701 (R).

Yossifon, G. & Chang, H.C. 2008 Selection of nonequilibrium overlimiting currents: universal depletion layer formation dynamics and vortex instability. *Phys. Rev. Lett.* **101** (25), 254501.

ZALTZMAN, B. & RUBINSTEIN, I. 2007 Electro-osmotic slip and electroconvective instability. *J. Fluid Mech.* **579**, 173–226.

ZHENG, J., KIM, M.S., TU, Z., CHOUDHURY, S., TANG, T. & ARCHER, L.A. 2020 Regulating electrodeposition morphology of lithium: towards commercially relevant secondary li metal batteries. *Chem. Soc. Rev.* **49** (9), 2701–2750.